Focus Section: Arctic and Antarctic Seismology

Remote Triggering of Icequakes at Mt. Erebus, Antarctica by Large Teleseismic Earthquakes

Chenyu Li[*1], Zhigang Peng[1], Julien A. Chaput[2], Jacob I. Walter[3], and Richard C. Aster[4]

Abstract

Recent studies have shown that the Antarctic cryosphere is sensitive to external disturbances such as tidal stresses or dynamic stresses from remote large earthquakes. In this study, we systematically examine evidence of remotely triggered microseismicity around Mount (Mt.) Erebus, an active high elevation stratovolcano located on Ross Island, Antarctica. We detect microearthquakes recorded by multiple stations from the Mt. Erebus Volcano Observatory Seismic Network one day before and after 43 large teleseismic earthquakes, and find that seven large earthquakes (including the 2010 M_w 8.8 Maule, Chile, and 2012 M_w 8.6 Indian Ocean events) triggered local seismicity on the volcano, with most triggered events occurring during the passage of the shorter-period Rayleigh waves. In addition, their waveforms and locations for the triggered events are different when comparing with seismic events arising from the persistent small-scale eruptions, but similar to other detected events before and after the mainshocks. Based on the waveform characteristics and their locations, we infer that these triggered events are likely shallow icequakes triggered by dilatational stress perturbations from teleseismic surface waves. We show that teleseismic earthquakes with higher peak dynamic stress changes are more capable of triggering icequakes at Mt. Erebus. We also find that the icequakes in this study are more likely to be triggered during the austral summer months. Our study motivates the continued monitoring of Mount Erebus with dense seismic instrumentation to better understand interactions between dynamic seismic triggering, crospheric processes, and volcanic activity.

Cite this article as Li, C., Z. Peng, J. A. Chaput, J. I. Walter, and R. C. Aster (2021). Remote Triggering of Icequakes at Mt. Erebus, Antarctica by Large Teleseismic Earthquakes, *Seismol. Res. Lett.* **XX**, 1–10, doi: 10.1785/0220210027.

Supplemental Material

Introduction

At present, about 10% of Earth's continental surface is covered by glaciers, ice caps, and ice sheets. However, because of global climate change, this number is rapidly diminishing, particularly in temperate mountain regions. Antarctica and Greenland are, overwhelmingly, the two major continental regions hosting glacial ice, encompassing more than 97% of Earth's glacial area (Aster and Winberry, 2017). Studying Earth's cryosphere is crucial because cryospheric change is anticipated to have accelerating direct influence on the biosphere and human life, notably including effects on weather, water availability, and sea level rise (i.e., Pörtner *et al.*, 2019). Thanks to an increasing deployment of geophysical instruments and collection of data over the last decade (i.e., Global Navigation Satellite Systems, seismology, Interferometric Synthetic Aperture Radar) in cryospheric regions, we have a much-improved characterization and understanding of cryosphere-related seismic activity. The cryosphere hosts a rich and complex variety of seismogenic processes (i.e., Aster and Winberry, 2017; Garcia *et al.*, 2019), including those related to surface ice dynamics (i.e., icequakes, surface crevassing), ice–rock interactions (basal stick-slip events), and interaction with water (i.e., basal crevasse flow, hydraulic tremor). Among them, icequakes produce similar short-duration seismic vibrations or sometimes loud booms at the ground surface such as shallow earthquakes, but the driving mechanisms are quite different. Glacial seismology or cryoseismology provides an efficient way to image seismic structures within and below ice layers, and monitor cryospheric activities with seismic observations, such as rapid glacier movement (Podolskiy and Walter, 2016).

1. School of Earth & Atmospheric Sciences, Georgia Institute of Technology, Atlanta, Georgia, U.S.A., https://orcid.org/0000-0002-0442-6928 (CL); 2. Department of Geological Sciences, University of Texas at El Paso, El Paso, Texas, U.S.A.; 3. Oklahoma Geological Survey, University of Oklahoma, Norman, Oklahoma, U.S.A., https://orcid.org/0000-0001-7127-9422 (JIW); 4. Department of Geosciences and Warner College of Natural Resources, Colorado State University, Fort Collins, Colorado, U.S.A., https://orcid.org/0000-0002-0821-4906 (RCA)

*Corresponding author: lchenyu1992@gmail.com

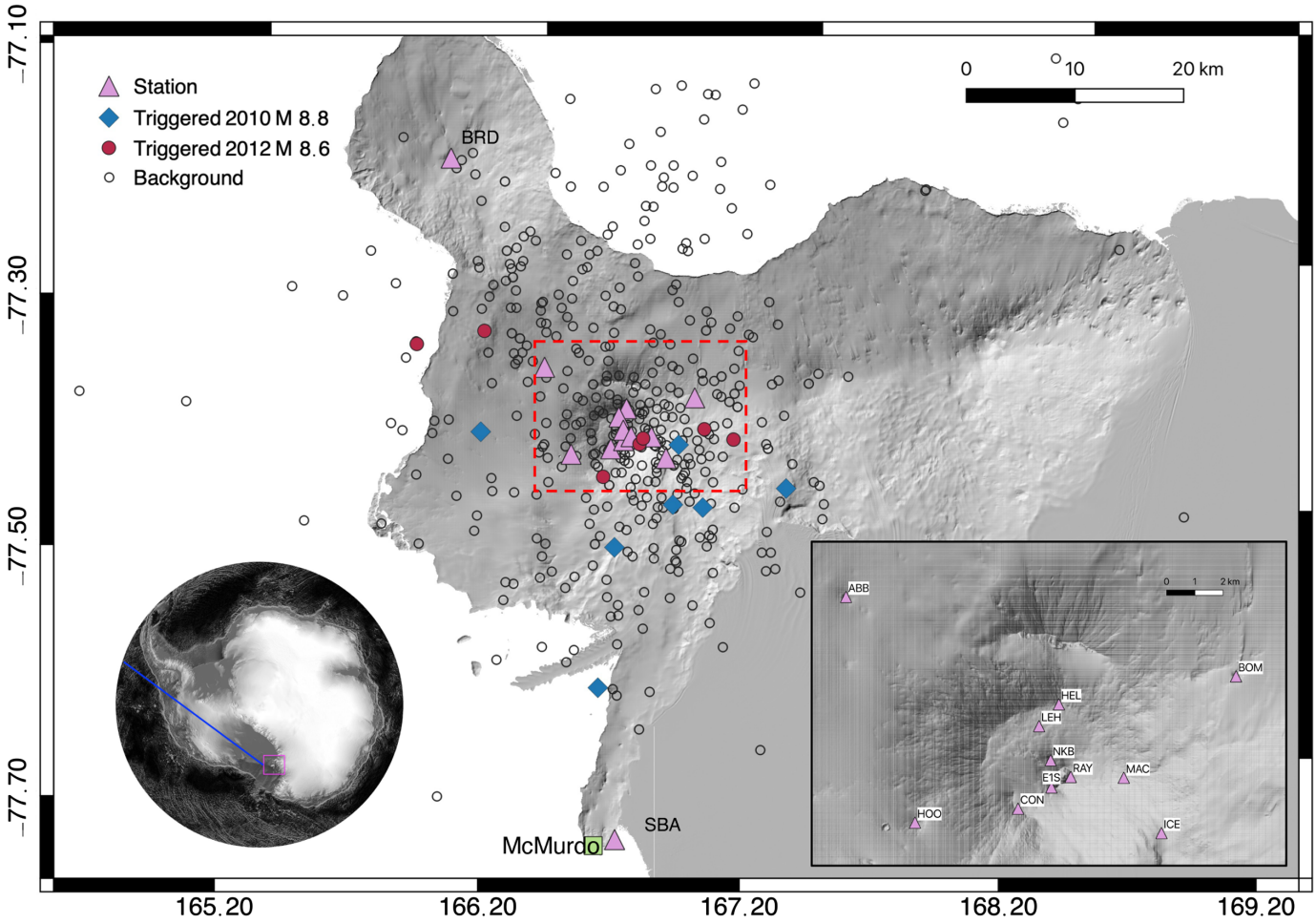

Figure 1. Seismic stations (pink triangles) around Mt. Erebus, Ross Island, and McMurdo Station (United States), and the locations of Global Seismographic Network broadband station SBA. Open circles, blue diamonds, and red circles mark detected local background seismic events, and those triggered by the 2010 M_w 8.8 Maule and 2012 M_w 8.6 Indian Ocean earthquakes, respectively. (Left inset) The surface-wave ray path from the 2010 M_w 8.8 Maule earthquake seismic waves to Mt. Erebus. (Right inset) Seismic stations around the crater region. The color version of this figure is available only in the electronic edition.

Recent studies have found that the Antarctic cryosphere is sensitive to external disturbances such as waves and tidal stresses, ocean tidal stresses (e.g., MacAyeal *et al.*, 2009; Brunt *et al.*, 2011; Zoet *et al.*, 2012; Walker *et al.*, 2013; Chen *et al.*, 2019; Aster *et al.*, 2021). Large earthquakes are well documented to be capable of triggering fault slip in remote regions through the transient dynamic stress changes induced by transient teleseismic waves (e.g., Kane *et al.*, 2007; Pollitz *et al.*, 2012; Hill and Prejean, 2015; Alfaro-Diaz *et al.*, 2020). Peng *et al.* (2014) identified widespread dynamic triggering of shallow icequakes in West Antarctica and the Antarctica Peninsula during large-amplitude surface waves of the 27 February 2010 M_w 8.8 Maule, Chile, earthquake. However, limited by sparse station distributions, they were unable to accurately locate these seismic events to better understand their source mechanisms and triggering behaviors. Triggered basal stick-slip events at Whillans Ice Plain were also observed after the 2011 M_w 9.1 Tohoku earthquake (Walter *et al.*, 2013). Previous studies have found that geothermal and volcanic regions are more sensitive to dynamic triggering than other regions (Brodsky and Prejean, 2005; Aiken and Peng, 2014; Hill and Prejean, 2015; Fan *et al.*, 2021). A glaciated volcano with a dense seismic network likely provides one of the best opportunities to decipher how earthquakes, volcanoes, and cryospheric activities interact with each other.

In this study, we examine evidence of remotely triggered microseismicity around Mount (Mt.) Erebus with multiple seismic stations during a 16 yr time period. Mt. Erebus is a large and high (3794 m, main crater with ~1 km diameter) active polygenetic stratovolcano that forms the bulk of Ross Island, Antarctica (Sims *et al.*, 2021). It is the southernmost active volcano on Earth and is located approximately 35 km from McMurdo Station (United States) and Scott Base (New Zealand) (Fig. 1). The eruption style on Mt. Erebus is relatively mild Strombolian type eruptions of gas slugs from an open-conduit magmatic system (Aster *et al.*, 2008; Gerst *et al.*, 2013) with a volcanic explosion index of 0–1 (out of 8). Eruptions across the past several decades have predominantly

originated at a long-lived phonolitic lava lake and can exceed 50 events per day during particularly active periods (e.g., Knox *et al.*, 2018), with infrequent phreatic explosions and small ash-rich eruptions from secondary vents (Jones *et al.*, 2008). The lava lake is associated with a near-summit and shallow magma body (several hundreds of meters below the surface) approximately 1 km northwest of the eruptive vents and Main Crater (Chaput *et al.*, 2012; Zandomeneghi *et al.*, 2013; Blondel *et al.*, 2018). With ongoing small-scale eruptions, persistent lava lakes, and longstanding monitoring infrastructure, the volcano is a natural laboratory to study volcanic processes and interactions between volcanoes, earthquakes, and cryospheric processes.

Data and Method

Short-period seismometers were widely deployed on and around Erebus volcano beginning in the 1980s. The ER network of short-period and broadband seismometers (Aster *et al.*, 2004) was maintained by the Mt. Erebus Volcano Observatory between 2002 and 2017. Temporary stations and dense arrays have also been deployed in recent years, providing high-quality seismic data for subsequent body wave and ambient noise imaging of the volcano (Zandomeneghi *et al.*, 2010; Chaput *et al.*, 2012, 2015, 2016; Blondel *et al.*, 2018). In this study, we use seismic data recorded by the permanent MEVO stations and the Global Seismographic Network broadband station IU.SBA near Scott Base.

Here, we conduct a systematic search for remotely triggered seismicity at Mt. Erebus from 2000 to 2017, during which time the volcano was notably well monitored by a telemetered (mixed short period and broadband) network (Aster *et al.*, 2004). We first select 56 $M_w > 7.0$ earthquakes with epicentral distances more than 1000 km that have predicted surface-wave dynamic stress changes larger than 1 kPa on station SBA. Predicted dynamic stress at SBA is computed with the following expression:

$$\log_{10} A_{20} = M_s - 1.66 \log_{10} \Delta - 2, \tag{1}$$

in which A_{20} (micrometers) is the peak dynamic strain of long-period (20 s) surface waves, and Δ is the epicentral distance in degrees (van der Elst and Brodsky, 2010). We retrieve archived continuous data one day before and after each distant mainshock. Among the 56 selected earthquakes, only 43 are recorded by multiple stations in the ER network. We run a recursive short-term-average/long-term-average (STA/LTA) method using the ObsPy coincidence trigger package (Beyreuther *et al.*, 2010; Megies *et al.*, 2011; Krischer *et al.*, 2015) on high-pass-filtered (2 Hz) vertical data recorded one-day before and after the 43 mainshocks. We use a 2 s short-term window and a 10 s long-term window, and the start and end of the trigger window for each channel are determined when the characteristic trigger function rises above 3 and falls below 1, respectively. The coincidence trigger package groups stations that have overlapping trigger windows, and we require at least three triggered stations to declare a detected event. The start time of the trigger window in the recursive STA/LTA trigger may slightly differ from the impulsive onset. Here, we use the Baer Picker (Baer and Kradolfer, 1987) in ObsPy to estimate the arrival times of newly detected events on all stations, and use the NonLinLoc software (Lomax *et al.*, 2001) to locate them. In the NonLinLoc method, we search for the best-fitting location with an oct-tree sampling algorithm, and the grids are centered at [167.10°E, 77.53°S], spanning from 40 km to the north to 30 km to the south, and from 20 km to the east to 50 km to the west, and 12 km from surface to depth. Here, we use a 1D velocity model from Dibble *et al.* (1994), and an elevation model with 8 m spatial resolution for the topography of Ross Island (Howat *et al.*, 2019).

We then evaluate the significance of seismicity rate increase by computing the Z and β statistical values with the catalog of candidate events (Habermann, 1983; Matthews and Reasenberg, 1988; Marsan and Nalbant, 2005; Aron and Hardebeck, 2009):

$$Z = \frac{N_a T_b - N_b T_a}{\sqrt{N_a T_b^2 + N_b T_a^2}}, \tag{2}$$

$$\beta = \frac{N_a - N(T_a/T)}{\sqrt{N(T_a/T)(1-(T_a/T))}}, \tag{3}$$

in which the N_a and N_b are the number of events in the triggering time window T_a after and the time window T_b before the distant mainshock, respectively, and $N = N_a + N_b$. The T_a used here is the time window from the P-wave arrival of the distant mainshocks to the end of the surface wave that corresponds to the apparent velocity of 2 km/s at station IU.SBA, and T_b is a one day time window before the mainshock origin time. The definitions of the Z- and β-values are highly similar, with the Z-value being more symmetric than the β-value. Both the Z- and β-values are based on the assumption of Poisson-distributed earthquake sequences, and they both approximately follow the standard normal distribution under such assumptions. Previous studies have shown that β- and Z-values above 2 generally indicate statistically significant seismicity rate increases (e.g., Hill and Prejean, 2015; Aiken *et al.*, 2018; Pankow and Kilb, 2020).

At Mt. Erebus, the high-pass-filtered waveforms of different event types (e.g., Strombolian eruptions, icequakes, or human-made explosions) often appear to be highly similar on stations more than a few kilometers away due to an exceptional degree of high-frequency seismic scattering reflecting the extreme heterogeneity of the upper volcanic edifice (e.g., Chaput *et al.*, 2012, 2015). We compare the origin time of detected events with an eruption catalog of 2999 events between 2003 and 2012 (Knox *et al.*, 2018) and identify events that are detected

within 5 s of known eruptions. For the remote mainshocks after 2012, we run a matched filter detection with stacked waveforms from 18 eruptions during 2006 for the one-day window before and after the mainshocks to generate the eruption catalog for this period. This is the same template termed "boomer" by Knox *et al.* (2018; Fig. S1, available in the supplemental material to this article). A single template is lava lake eruptions because their seismic and infrasonic waveforms are highly repetitive (e.g., Aster *et al.*, 2003) and have a characteristic moveout across the network. The matched filter method cross-correlates waveforms of template events with continuous waveforms to search for similar events (e.g., Peng and Zhao, 2009; Meng and Peng, 2014). The template and continuous waveforms are band-pass filtered between 2 and 8 Hz to ensure a good signal-to-noise ratio. We use a cross-correlation (CC) threshold of 0.15 and 10 times the median absolute deviation above the daily median CC trace to discriminate events that have good waveform matches with the "boomer" template, and these are definitively identified as lava lake eruptions.

Results

With the STA/LTA method, we detect 7390 events one day before the origin time, and 213 events during the surface-wave windows of 43 distant mainshocks (Tables S1 and S2). Next, we examine which distant mainshocks show statistical evidence for triggered microseismicity using computed β and Z metrics. The comparison for β- and Z-values (Fig. 2) using the same predefined time windows shows that the β-value systematically exceeds the Z-value. There are four earthquakes with $\beta > 2$, whereas none of the corresponding Z-values are above 2. For the two earthquakes with $\beta > 2.2$ (the 27 February 2010 M_w 8.8 Chile and 11 April 2012 M_w 8.6 Indian Ocean earthquakes), their Z-values are above 1.65, which exceeds the 90% significant level of deviation under the standard normal distribution. Therefore, in this study these two events are considered as positive dynamic triggering cases.

The most robust evidence of triggered seismicity at Mt. Erebus is observed during the surface waves of the 27 February 2010 M_w 8.8 Maule, Chile, earthquake ($N_a = 6$, $N_b = 28$). In Figure 3b,c, the high-pass-filtered waveforms correspond to high-frequency seismic signals recorded by multiple stations during the surface waves of the Maule mainshock. The continuous wavelet transform (CWT) of unfiltered data separates both high-frequency local signals and low-frequency signals from the mainshock, with local signals being mainly limited to long-period (~16 s) Rayleigh waves driven by dilatational stress perturbations (Fig. 3d). For the 11 April 2012 M_w 8.6 Indian Ocean earthquake ($N_a = 12$, $N_b = 130$), although the background seismicity is relatively high, the corresponding Z and β statistical values suggest that there is also a significant increase of seismicity at Mt. Erebus during its teleseismic waves (Fig. 3).

In addition, 30 teleseismic earthquakes have at least one local event detected during the passage of the surface waves,

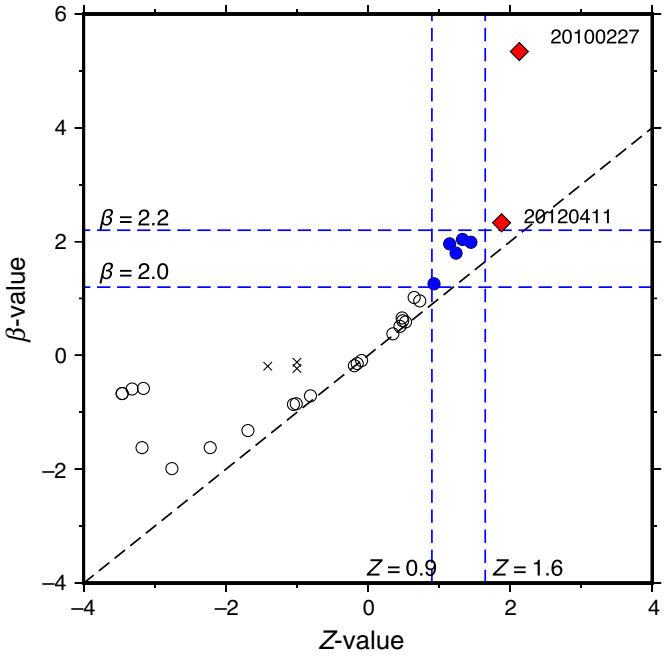

Figure 2. Comparison of β and Z statistic values for teleseismic earthquakes with $-4 < Z < 6$. Blue dashed lines mark thresholds used in this study. Red diamonds mark two high-confidence positive dynamic triggering cases and blue circles mark five possible dynamic triggering cases (Fig. 6). The three crosses mark events with $N_a + N_b < 5$. The black dashed line marks the 1:1 relationship. The color version of this figure is available only in the electronic edition.

suggesting lower-level surface-wave-triggered seismicity at Mt. Erebus (Table S1). However, the persistent high-frequency signals, indicating high-seismicity rates before the mainshocks, along with high background noise and data gaps in the waveforms shortly after some mainshocks, makes it difficult to conclude that these events are dynamically triggered. For example, there are clear local events detected by multiple stations (Fig. 4) during the surface waves of the 23 December 2004 M_w 8.1 Macquarie Island ($N_a = 3$, $N_b = 77$) and 2 March 2016 M_w 7.8 South Sumatra earthquake ($N_a = 5$, $N_b = 59$), but the β- and Z-values are less than our threshold of $\beta > 2.2$ (and $Z > 1.65$) for dynamic triggering. Based on the statistical values and visual inspection of the waveforms after the arrival of mainshock surface waves, we classify these teleseismic earthquakes with $\beta > 1.2$ (or $Z > 0.9$) as possible dynamic triggering cases in this study (Fig. 2). Figures S2 and S3 show three additional earthquakes with possible dynamic triggering at Mt. Erebus: the 6 February 2013 M_w 8.0 and 8 December 2016 M_w 7.8 Solomon Islands earthquakes, 3 May 2006 M_w 8.0 Tonga earthquake, and the 26 December 2004 M_w 9.1 Sumatra earthquake, which has no clear evidence of triggering. The waveforms and cumulative number of events for positive and possible triggering teleseismic earthquakes are shown in Figures S4–S7.

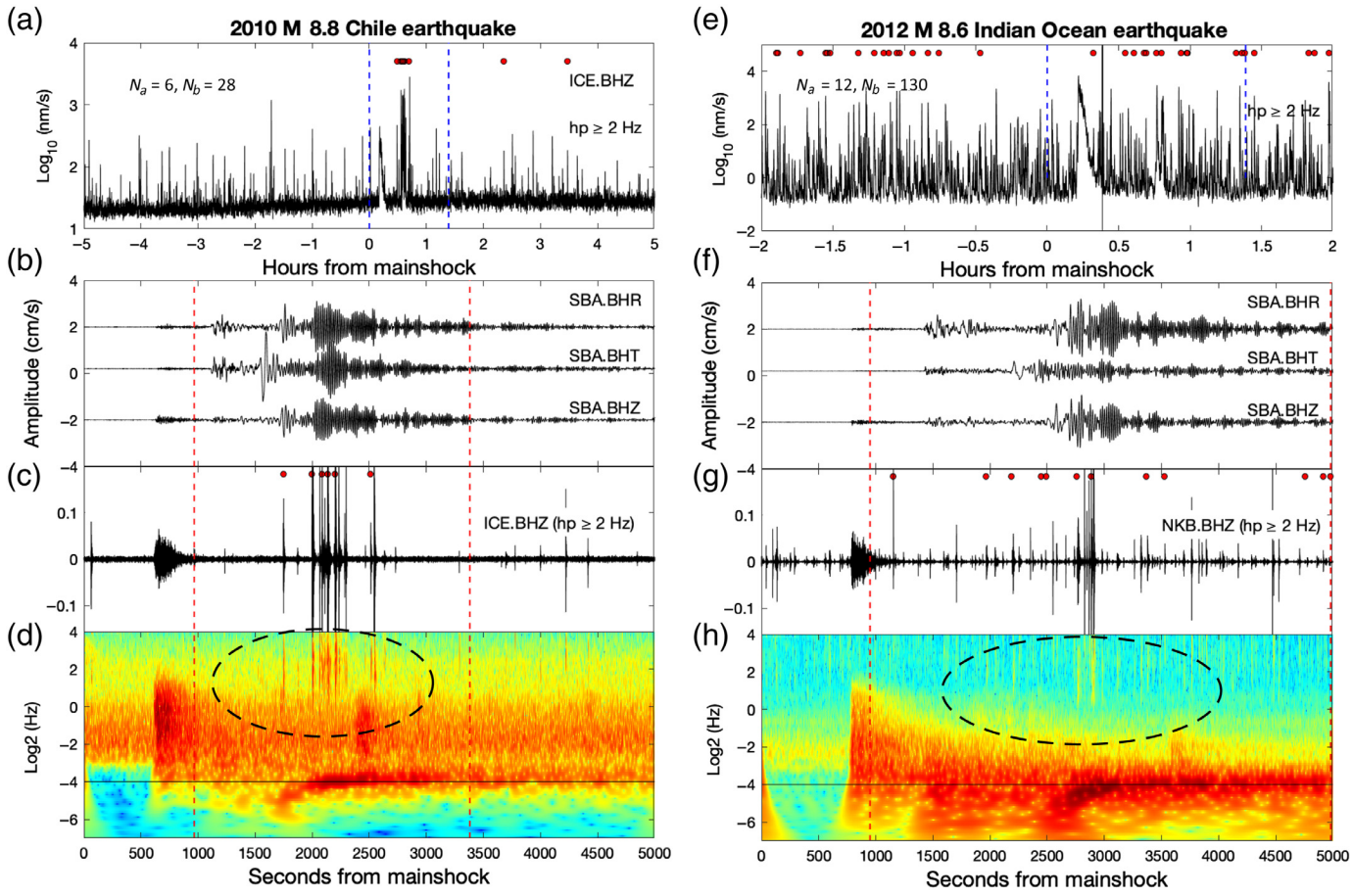

Figure 3. (a) 2 Hz high-pass-filtered envelope function obtained using the Hilbert transform for 5 hr before and after the 27 February 2010 M_w 8.8 Maule, Chile, mainshock at station ICE. Red circles mark the events detected and located in this study, dashed blue lines are the zoom-in time window in (b)–(d). (b) Unfiltered three-component waveforms in SBA during the Maule mainshock. (c) High-pass-filtered waveform and (d) continuous wavelet transform of the vertical component showing both long-period signals from the Maule mainshock and local high-frequency signals. We have circled the high-frequency signals for readers to find them easily. The gliding signal starting around 1700 s corresponds to the dispersive surface wave of the mainshock. The black line in (d) marks the period of 16 s. (e)–(h) The same plots for the 11 April 2012 M_w 8.6 Indian Ocean earthquake. Dashed red lines are the triggering time window. The color version of this figure is available only in the electronic edition.

For the two positive and four possible triggering mainshocks, we detect and locate 523 events, which include 219 and 304 events one day before and after the mainshock origin times respectively (Table S3). Locations of these events, which are scattered around the volcano, are shown in Figure 1. There are some events scattered below the ocean floor, which is likely caused by the poor constraint on the locations outside the network. We also manually pick the arrival times of 16 triggered events during surface waves of 2010 M_w 8.8 Chile and 2011 M_w 8.6 Indian Ocean earthquake, and most of them (14 out of 16) are distributed on the east–southeast side of the volcano (Fig. 1). Previous studies showed that icequakes outside crater region are mainly distributed on the steep and heavily glaciated south side of the volcano (Knox, 2012). Therefore, we expect that the triggered events are more likely to be located on the south side of the volcano. However, this is inconsistent with the observed locations in this study. This is likely caused by location uncertainties. Because we mostly use *P* wave only, and the stations are mostly distributed in a tight cluster around the volcanic rim, the location uncertainties might be relatively higher.

Peng *et al.* (2014) found that the triggered icequakes by 2010 M_w 8.8 Chile earthquake are not similar to other background events. To examine waveform similarities for these detected events, we compute the mean CC value between all possible event pairs before and after the teleseismic earthquakes. Specifically, we use a 17 s time window starting 2 s before the automatically picked *P* arrival on the 2 Hz high-pass-filtered seismogram. For the 2010 M_w 8.8 and 2012 M_w 8.6 earthquakes, and two other possible cases (the 6 February 2013 M_w 8.0 and 2 March 2016 M_w 7.8 earthquakes) of dynamic triggering, the similarities between triggered events are not clearly above the similarities with the background events (Fig. S8). We also compute the CC value of the triggered

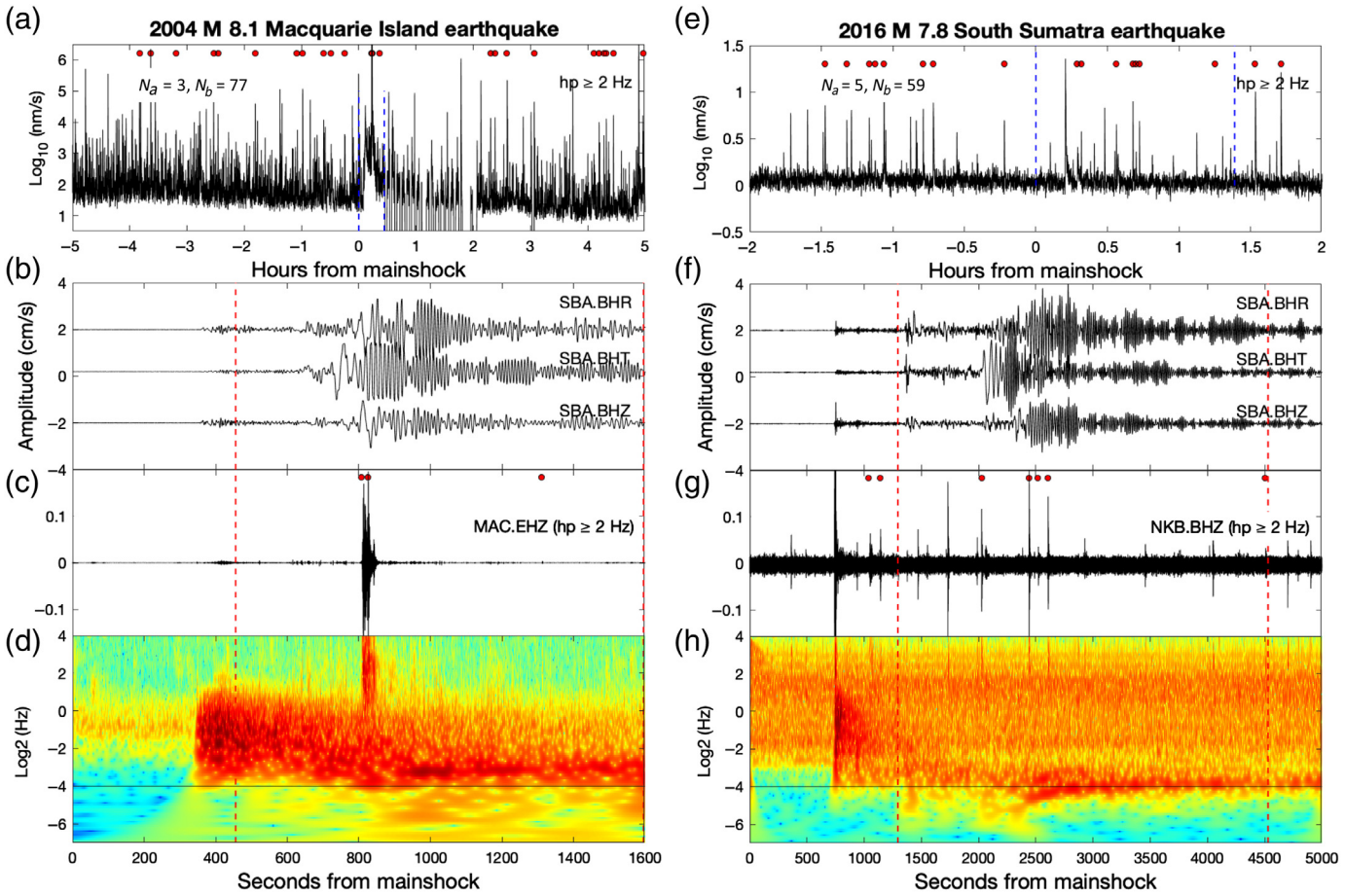

Figure 4. Same as Figure 3 for the 23 December 2004 M_w 8.1 Macquarie Islands earthquake and 2 March 2016 M_w 7.8 South Sumatra earthquake. The color version of this figure is available only in the electronic edition.

events after 2010 M_w 8.8 Chile and 2012 M_w 8.6 Indian Ocean earthquakes with eruption "boomer" template, and the CC values for most events are lower than 0.1, suggesting that the triggered events are distinct from eruptions. The waveforms of some events before the 2010 M_w 8.8 Chile earthquake and triggered events during surface waves are shown in Figure S9. We compare the frequency content with amplitude spectra for the triggered events by 27 February 2010 M_w 8.8 Chile earthquake and 11 April 2012 M_w 8.6 Indian earthquake, and find no systematic change of frequency for the triggered events with respect to mainshocks (Fig. S10). Furthermore, the waveforms of triggered events do not show clear evolution with the time to mainshocks (Fig. S11). The peak amplitudes of 2 Hz high-pass-filtered waveforms contain variations, but they are not directly related to the time from mainshock (Tables S4 and S5).

We estimate the local peak dynamic stress change (σ) for signals from teleseismic earthquakes (e.g., Aiken and Peng, 2014; Hill and Prejean, 2015) using

$$\sigma = \frac{\mu(\mathrm{PGV})}{V_{\mathrm{ph}}}, \tag{4}$$

in which μ is the shear rigidity, V_{ph} is the phase velocity of the passing seismic wave, and PGV is the peak ground velocity measured from the vertical-component seismogram after removing the instrument response at broadband station SBA. Here, we use $\mu = 30$ GPa, and $V_{\mathrm{ph}} = 3$ km/s as the Rayleigh-wave velocity. As shown in Figure 5a, the dynamic stress change caused by the 11 April 2012 M_w 8.6 and 27 February 2010 M_w 8.8 earthquakes are around the common threshold of triggering observed in other regions (5–10 KPa; Brodsky and Prejean, 2005; Aiken and Peng, 2014; Hill and Prejean, 2015). However, three out of five events with possible triggering are clearly below this threshold. No clear dependency is observable on either the epicentral distance or azimuth of the triggering mainshocks, likely due to the paucity of triggering mainshocks (Fig. 5a,c).

Discussion

After examining 43 teleseismic earthquakes for dynamic triggering at Mt. Erebus and removing seven events with $N_a + N_b < 5$ in the analysis, we identify two earthquakes that have clear evidence of dynamic triggering (5.5%), and five events with possible evidence of dynamic triggering (13.9%).

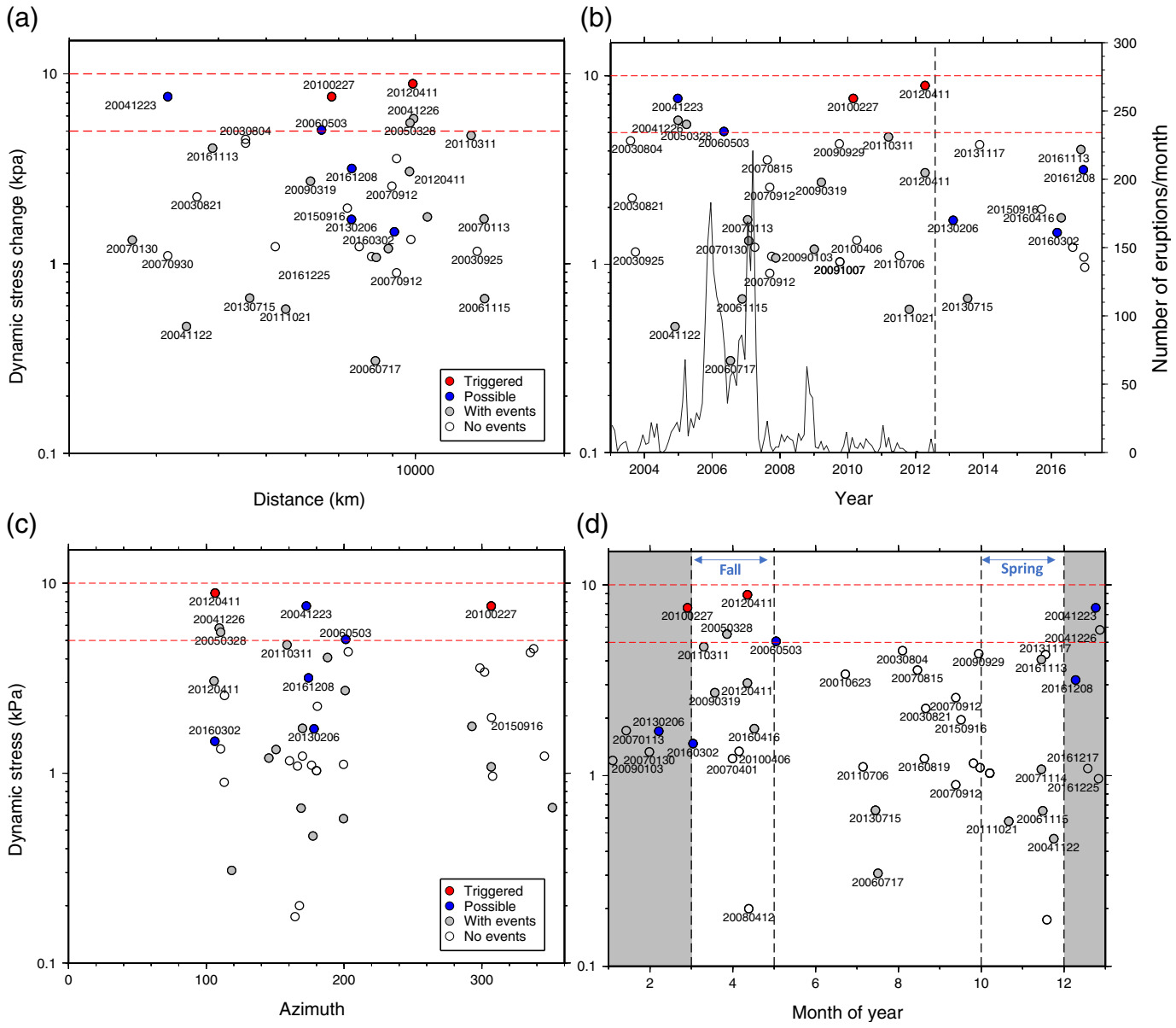

Figure 5. (a) Estimated dynamic stress changes from the peak ground velocities on station SBA versus distances for all 43 teleseismic earthquakes analyzed in this study. The remote earthquakes with positive and possible triggering are marked as red and blue circles, respectively. (b) Peak dynamic stress change estimates (van der Elst and Brodsky, 2010) for 43 distant earthquakes with calendar times indicated. Eruptions per month from 2003 to 2012 (Knox *et al.*, 2018) are marked by the thin black lines, and the thin black dashed line indicate the end of the eruption catalog. (c) Dynamic stress changes versus azimuth from all distant earthquakes. (d) Dynamic stress change and month of the year, the austral summer is indicated by the gray shaded area, and austral fall and spring are marked. The color version of this figure is available only in the electronic edition.

The three earthquakes with highest peak dynamic stress changes all have positive or possible dynamic triggered events at Mt. Erebus. During the 2010 M_w 8.8 Maule, Chile, earthquake, most local events occurred during or right after the 16 s Rayleigh wave. For the 2012 M_w 8.6 Indian Ocean earthquake, the local high-frequency energy was also more intense during its Rayleigh wave. The amplitude spectra show that the 2010 M_w 8.8 earthquake and 2012 M_w 8.6 earthquake are most significant in the frequency range 0.05–0.1 Hz (10–20 s; Fig. 6). Based on the limited observation of teleseismic earthquakes with dynamic stress changes between 5 and 10 kPa, we argue that the peak dynamic stress change might play an important role in dynamic triggering by promoting failure in zones that are critically stressed. We note that the dynamic stress in the ice layer on the surface of Mt. Erebus might be different from the estimated ones based on rock properties, but the wavelengths of long-period (>16 s) surface waves could be more than 10 km, thus they could propagate at the medium deeper than the thin ice layers. If we use the $\mu = 3$ GPa, and $V_{ph} =$ 2 km/s as the shear modulus and surface-wave velocity in ice,

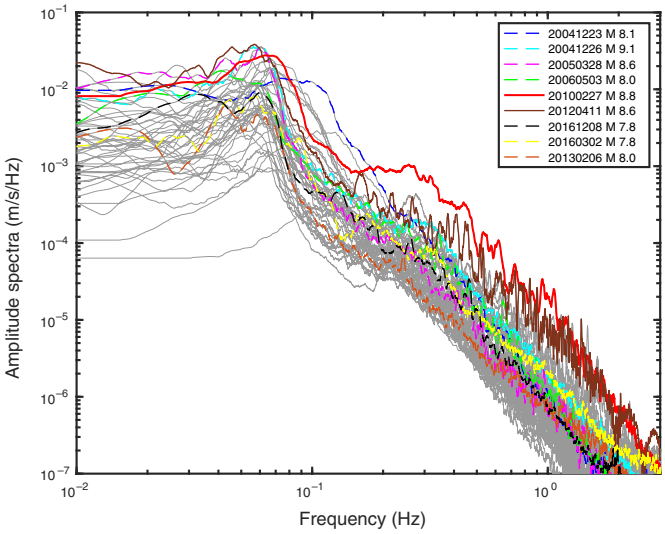

Figure 6. Amplitude spectra for all teleseismic earthquakes observed at station SBA, highlighting events of interest. The two positive triggering earthquakes are marked as solid colored lines, and five possible triggering earthquakes are marked as dashed colored lines. The color version of this figure is available only in the electronic edition.

the estimated dynamic stresses will be systematically lower, but the relative values are the same for different earthquakes (Fig. S12). The 5–10 kPa dynamic stress threshold for volcanoes and geothermal regions (Brodsky and Prejean, 2005; Aiken and Peng, 2014; Hill and Prejean, 2015) is a broad estimate, and for triggered event in Mt. Erebus, the threshold is probably lower because ice is generally weaker than rocks.

In a glaciated volcano with active eruptions, discriminating between icequakes, tectonic earthquakes and eruption events is crucial for understanding the origin of local seismicity. In this study, we first rule out the possibility that the triggered events are eruptions. The numbers of eruptions in the two-day window around all the earthquakes are low, usually less than 2 (Table S1). The eruption catalog from 2003 to 2012 is a relatively complete catalog based on a matched filter detection (Knox *et al.*, 2018). For the earthquakes after 2013, our matched-filter detection only identifies three eruptions after the 16 April 2016 M_w 7.8 earthquake. The CC values between triggered events and the eruption template are also smaller than 0.1. Therefore, these eruption events were not the primary sources of the high-frequency signals observed in this study. Second, the locations of the triggered events are around but not on top of the crater, suggesting that they are not eruption-type events associated with the crater, which is the only region of the volcano with active events (e.g., Jones *et al.*, 2008). Although the depth of an event would typically be a robust way to classify its event type, the depths of our detected events in our study are not well constrained, mainly because most of the events are located with only *P*-phase arrivals and due to the sparsity of the network.

The transient dynamic stress from teleseismic earthquakes might also affect the near-summit magma chamber northwest of the lava lake (Zandomeneghi *et al.*, 2013) and cause magma overpressure and volcanic-tectonic seismicity (Hill and Prejean, 2015; Namiki *et al.*, 2016; Liu *et al.*, 2017, 2021). However, during 2010 M_w 8.8 and 2012 M_w 8.6 earthquakes, the eruption rate was low and the volcano did not show any increase of eruption activity after the mainshocks (Fig. 5b; Table S1). Eruptive activity at Mt. Erebus is highly variable from year to year and was particularly high between 2006 and 2007. Unfortunately, the teleseismic earthquakes that occurred during this time period had relatively low dynamic stress changes and are not considered as likely to trigger seismicity (Fig. 5b). On the other hand, there were some detected local events during the teleseismic surface waves of the 2006–2007 earthquakes. Hence, it is also possible that the background noise was high due to wind-related noise, thus making it more difficult to identify dynamic triggering during these earthquakes. There is also a lack of volcano-tectonic seismic sources on Mt. Erebus, which is likely caused by an open conduit and resultant ongoing degassing and lack of internal deviatoric stress (e.g., Rowe *et al.*, 2000; Aster *et al.*, 2003). Therefore, the triggered events are not likely to be volcanic-tectonic seismicity.

Based on our observations, we argue that the teleseismic surface-wave-triggered events around Mt. Erebus are likely shallow icequakes within brittle ice that are similar to those noted as being teleseismically triggered near other Antarctic seismic stations by Peng *et al.* (2014). Previous studies (Knox, 2012) found that 43% of background near-summit icequakes at Mt. Erebus occur during the austral fall (March to May), and 30% during austral spring (October to December). Both of these winter–summer shoulder seasons have large seasonally evolving air temperature changes because of the polar latitude and high altitude of Mt. Erebus that likely increase thermal stresses in shallow ice. In our study, two high-confidence and five possible dynamic triggering teleseismic events (Fig. 5d) all occurred within austral spring, summer, or fall, motivating the hypothesis that icequakes on the volcano may be more easily triggered when the ambient temperature is relatively high or seasonally changing, or during periods of elevated background icequake occurrence. However, we note that during the Antarctic winter (May to October), we do not have any distant mainshocks that produced dynamic stress changes larger than 5 KPa during our analyzed time period, so this hypothesis is poorly tested by these data. Future studies could resolve this by expanding the time of observation and by investigating if any smaller, but closer earthquakes might produce sufficient dynamic stresses to trigger local icequakes on Mt. Erebus.

Conclusion

We systematically analyzed remote dynamic triggering behavior at Mt. Erebus in Antarctica by studying seismograms from

43 teleseismic earthquakes between 2000 and 2017. We find that two (5.5%) of these earthquakes triggered local seismic events that were detected by the Mt. Erebus Volcano Observatory Seismic Network. The waveform characteristics and source locations of high confidence of triggered events during the 2010 M_w 8.8 Chile and 2012 M_w 8.6 Indian Ocean earthquakes indicate that these events are likely shallow icequakes, which have been previously observed to occur at high elevations of the volcano. Teleseismic earthquakes that produce higher dynamic stress changes are more likely to trigger icequakes, and triggering is less likely to be observed during the Antarctic winter during this time period, although the seasonal sampling is poor. Further observations of large teleseismic earthquakes that generate high dynamic stress changes in glaciated regions can provide more insight into how and where icequakes occur and how they are affected by external seismic perturbation.

Data and Resources

The facilities of Incorporated Research Institutions for Seismology (IRIS) Data Services, and specifically the IRIS Data Management Center, were used for access to waveforms, related metadata, and/or derived products used in this study. The seismic data analyzed in this article is downloaded from IRIS Data Management Center (http://ds.iris.edu/mda/ER/, last accessed December 2020). The seismic data are processed with Seismic Analysis Code (SAC) and ObsPy python package. Figures in this article are generated with Generic Mapping Tools (GMT), QGIS, and MATLAB. The supplemental figures and tables are in the supplemental material.

Declaration of Competing Interests

The authors acknowledge there are no conflicts of interest recorded.

Acknowledgments

The authors thank the Mount Erebus Volcano Observatory Seismic Network for deploying and maintaining the seismic network. The authors appreciate Incorporated Research Institutions for Seismology (IRIS) Data Management Center for making these data available to the public. This article benefits from suggestions from *SRL* Editor-in-Chief Allison Bent, Guest Editor Myrto Pirli, Peter Voss, Reviewer Debi Kilb, and one anonymous reviewer. This work is supported by National Science Foundation (NSF) Grants EAR-1543399 (C. L. and Z. P.) and EAR-1745135 (J. W.). The IRIS Data Services are funded through the Seismological Facilities for the Advancement of Geoscience (SAGE) Award of the National Science Foundation under Cooperative Support Agreement EAR-1851048.

References

Aiken, C., and Z. Peng (2014). Dynamic triggering of microearthquakes in three geothermal/volcanic regions of California, *J. Geophys. Res.* **119,** 6992–7009.

Aiken, C., X. Meng, and J. Hardebeck (2018). Testing for the 'predictability' of dynamically triggered earthquakes in The Geysers geothermal field, *Earth Planet. Sci. Lett.* **486,** 129–140.

Alfaro-Diaz, R., A. A. Velasco, K. L. Pankow, and D. Kilb (2020). Optimally oriented remote triggering in the Coso geothermal region, *J. Geophys. Res.* **125,** e2019JB019131, doi: 10.1029/2019JB019131.

Aron, A., and J. L. Hardebeck (2009). Seismicity rate changes along the central California coast due to stress changes from the 2003 M 6.5 San Simeon and 2004 M 6.0 Parkfield earthquakes, *Bull. Seismol. Soc. Am.* **99,** 2280–2292.

Aster, R., and J. Winberry (2017). Glacial seismology, *Rep. Progr. Phys.* **80,** 126801.

Aster, R. C., B. P. Lipovsky, H. M. Cole, P. D. Bromirski, P. Gerstoft, A. Nyblade, D. A. Wiens, and R. Stephen (2021). Swell-triggered seismicity at the near-front damage zone of the Ross Ice Shelf, *Seismol. Res. Lett.*, doi: 10.1785/0220200478.

Aster, R., W. MacIntosh, P. Kyle, R. Esser, B. Bartel, N. Dunbar, J. Johnson, R. Karstens, C. Kurnik, and M. McGowan (2004). Real-time data received from Mount Erebus volcano, Antarctica, *Eos Trans. AGU* **85,** 97–101.

Aster, R., S. Mah, P. Kyle, W. McIntosh, N. Dunbar, J. Johnson, M. Ruiz, and S. McNamara (2003). Very long period oscillations of Mount Erebus Volcano, *J. Geophys. Res.* **108,** no. B11, 2522, doi: 10.1029/2002JB002101.

Aster, R., D. Zandomeneghi, S. Mah, S. McNamara, D. Henderson, H. Knox, and K. Jones (2008). Moment tensor inversion of very long period seismic signals from Strombolian eruptions of Erebus Volcano, *J. Volcanol. Geoth. Res.* **177,** 635–647.

Baer, M., and U. Kradolfer (1987). An automatic phase picker for local and teleseismic events, *Bull. Seismol. Soc. Am.* **77,** 1437–1445.

Beyreuther, M., R. Barsch, L. Krischer, T. Megies, Y. Behr, and J. Wassermann (2010). ObsPy: A Python toolbox for seismology, *Seismol. Res. Lett.* **81,** 530–533.

Blondel, T., J. Chaput, A. Derode, M. Campillo, and A. Aubry (2018). Matrix approach of seismic imaging: Application to the Erebus volcano, Antarctica, *J. Geophys. Res.* **123,** 10,936–10,950.

Brodsky, E. E., and S. G. Prejean (2005). New constraints on mechanisms of remotely triggered seismicity at Long Valley Caldera, *J. Geophys. Res.* **110,** no. B04302, doi: 10.1029/2004JB003211.

Brunt, K. M., E. A. Okal, and D. R. MacAyeal (2011). Antarctic ice-shelf calving triggered by the Honshu (Japan) earthquake and tsunami, March 2011, *J. Glaciol.* **57,** 785–788.

Chaput, J., M. Campillo, R. Aster, P. Roux, P. Kyle, H. Knox, and P. Czoski (2015). Multiple scattering from icequakes at Erebus volcano, Antarctica: Implications for imaging at glaciated volcanoes, *J. Geophys. Res.* **120,** 1129–1141.

Chaput, J., V. Clerc, M. Campillo, P. Roux, and H. Knox (2016). On the practical convergence of coda-based correlations: A window optimization approach, *Geophys. J. Int.* **204,** 736–747.

Chaput, J., D. Zandomeneghi, R. Aster, H. Knox, and P. Kyle (2012). Imaging of Erebus volcano using body wave seismic interferometry of Strombolian eruption coda, *Geophys. Res. Lett.* **39,** L07304 , doi: 10.1029/2012GL050956.

Chen, Z., P. Bromirski, P. Gerstoft, R. A. Stephen, W. S. Lee, S. Yun, S. Olinger *et al.* (2019). Ross ice shelf icequakes associated with ocean gravity wave activity, *Geophys. Res. Lett.* **46,** 8893–8902, doi: 10.1029/2019GL084123.

Dibble, R. R., B. O'Brien, and C. A. Rowe (1994). The velocity structure of Mount Erebus, Antarctica, and its Lava Lake, in

Volcanological and Environmental Studies of Mount Erebus, Antarctica, P. R. Kyle (Editor), Vol. 66, Antarctic Research Series.

Fan, W., A. J. Barbour, E. S. Cochran, and G. Lin (2021). Characteristics of frequent dynamic triggering of microearthquakes in southern California, *J. Geophys. Res.* **126,** e2020JB020820, doi: 10.1029/2020JB020820.

Garcia, L., K. Luttrell, D. Kilb, and F. Walter (2019). Joint geodetic and seismic analysis of surface crevassing near a seasonal glacier-dammed lake at Gornergletscher, Switzerland, *Ann. Glaciol.* **60,** no. 79, 1–13.

Gerst, A., M. Hort, R. C. Aster, J. B. Johnson, and P. R. Kyle (2013). The first second of volcanic eruptions from the Erebus volcano lava lake, Antarctica-Energies, pressures, seismology, and infrasound, *J. Geophys. Res.* **118,** no. 7, 3318–3340.

Habermann, R. E. (1983). Teleseismic detection in the Aleutian island arc, *J. Geophys. Res.* **88,** 5056–5064.

Hill, D. P., and S. Prejean (2015). Dynamic triggering, in *Treatise of Geophysics*, Second Ed., Vol. 4, 273–304.

Howat, I. M., C. Porter, B. E. Smith, M.-J. Noh, and P. Morin (2019). The reference elevation model of Antarctica, *Cryosphere* **13,** 665–674.

Jones, K. R., J. B. Johnson, R. Aster, P. R. Kyle, and W. McIntosh (2008). Infrasonic tracking of large bubble bursts and ash venting at Erebus volcano, Antarctica, *J. Volcanol. Geoth. Res.* **177,** 661–672.

Kane, D. L., D. Kilb, A. S. Berg, and V. G. Martynov (2007). Quantifying the remote triggering capabilities of large earthquakes using data from the ANZA Seismic Network catalog (southern California), *J. Geophys. Res.* **112,** no. B11.

Knox, H. A. (2012). Eruptive characteristics and glacial earthquake investigation on Erebus Volcano, Antarctica, *Ph.D. Thesis*, New Mexico Institute of Mining and Technology.

Knox, H. A., J. Chaput, R. Aster, and P. Kyle (2018). Multiyear shallow conduit changes observed with lava lake eruption seismograms at Erebus volcano, Antarctica, *J. Geophys. Res.* **123,** 3178–3196.

Krischer, L., T. Megies, R. Barsch, M. Beyreuther, T. Lecocq, C. Caudron, and J. Wassermann (2015). ObsPy: A bridge for seismology into the scientific Python ecosystem, *Comput. Sci. Discov.* **8,** 014003.

Liu, G., C. Li, Z. Peng, X. Li, and J. Wu (2017). Detecting remotely triggered microseismicity around Changbaishan Volcano following nuclear explosions in North Korea and large distant earthquakes around the world, *Geophys. Res. Lett.* **44,** 4829–4838.

Liu, G., C. Li, Z. Peng, Y. Liu, Y. Zhang, D. Liu, and M. Zhang (2021). The 2002–2005 Changbaishan volcanic unrest triggered by the 2002 M 7.2 Wangqing deep focus earthquake, *Front. Earth Sci.* **8,** 684.

Lomax, A., A. Zollo, P. Capuano, and J. Virieux (2001). Precise, absolute earthquake location under Somma–Vesuvius volcano using a new three-dimensional velocity model, *Geophys. J. Int.* **146,** 313–331.

MacAyeal, D. R., E. A. Okal, R. C. Aster, and J. N. Bassis (2009). Seismic observations of glaciogenic ocean waves (micro-tsunamis) on icebergs and ice shelves, *J. Glaciol.* **55,** no. 190, 193–206, doi: 10.3189/002214309788608679.

Marsan, D., and S. S. Nalbant (2005). Methods for measuring seismicity rate changes: A review and a study of how the M_w7.3 Landers earthquake affected the aftershock sequence of the M_w6.1 Joshua Tree earthquake, *Pure Appl. Geophys.* **162,** 1151–1185.

Matthews, M. V., and P. A. Reasenberg (1988). Statistical methods for investigating quiescence and other temporal seismicity patterns, *Pure Appl. Geophys.* **126,** 357–372.

Megies, T., M. Beyreuther, R. Barsch, L. Krischer, and J. Wassermann (2011). ObsPy—What can it do for data centers and observatories? *Ann. Geophys.* **54,** 47–58.

Meng, X., and Z. Peng (2014). Seismicity rate changes in the Salton Sea geothermal field and the San Jacinto fault zone after the 2010 M_w 7.2 El Mayor-Cucapah earthquake, *Geophys. J. Int.* **197,** 1750–1762.

Namiki, A., E. Rivalta, H. Woith, and T. R. Walter (2016). Sloshing of a bubbly magma reservoir as a mechanism of triggered eruptions, *J. Volcanol. Geoth. Res.* **320,** 156–171.

Pankow, K. L., and D. Kilb (2020). Going beyond rate changes as the sole indicator for dynamic triggering of earthquakes, *Sci. Rep.* **10,** 1–12.

Peng, Z., and P. Zhao (2009). Migration of early aftershocks following the 2004 Parkfield earthquake, *Nature Geosci.* **2,** 877–881.

Peng, Z., J. I. Walter, R. C. Aster, A. Nyblade, D. A. Wiens, and S. Anandakrishnan (2014). Antarctic icequakes triggered by the 2010 Maule earthquake in Chile, *Nature Geosci.* **7,** 677–681.

Podolskiy, E. A., and F. Walter (2016). Cryoseismology, *Rev. Geophys.* **54,** 708–758, doi: 10.1002/2016RG000526.

Pollitz, F. F., R. S. Stein, V. Sevilgen, and R. Bürgmann (2012). The 11 April 2012 east Indian Ocean earthquake triggered large aftershocks worldwide, *Nature* **490,** 250–253.

Pörtner, H.-O., D. C. Roberts, V. Masson-Delmotte, P. Zhai, M. Tignor, E. Poloczanska, K. Mintenbeck, A. Alegría, M. Nicolai, A. Okem, *et al.* (2019). IPCC special report on the Ocean and cryosphere in a changing climate, 755 pp.

Rowe, C., R. Aster, P. Kyle, R. Dibble, and J. Schlue (2000). Seismic and acoustic observations at Mount Erebus volcano, Ross island, Antarctica, 1994–1998, *J. Volcanol. Geoth. Res.* **101,** 105–128.

Sims, K., R. Aster, G. Gaetani, J. Blichert-Toft, E. Phillips, P. Wallace, G. Mattioli, D. Rasmussen, and E. Boyd (2021). *Mount Erebus Volcano: An Unparalleled Natural Laboratory to Study Alkaline Magmatism and Open-Conduit Volcano Behavior*, Geological Society of London Books, doi: 10.1144/M55-2019-8.

Van Der Elst, N. J., and E. E. Brodsky (2010). Connecting near-field and far-field earthquake triggering to dynamic strain, *J. Geophys. Res.* **115,** doi: 10.1029/2009JB006681.

Walker, C. C., J. N. Bassis, H. A. Fricker, and R. J. Czerwinski (2013). Structural and environmental controls on Antarctic ice shelf rift propagation inferred from satellite monitoring, *J. Geophys. Res.* **118,** 2354–2364.

Walter, J. I., Z. Peng, S. M. Tulaczyk, S. O'Neel, and J. M. Amundson (2013). Triggering of glacier seismicity (Icequakes) by distant earthquakes, *Seismol. Res. Lett.* **84,** 372.

Zandomeneghi, D., R. Aster, P. Kyle, A. Barclay, J. Chaput, and H. Knox (2013). Internal structure of Erebus volcano, Antarctica imaged by high-resolution active-source seismic tomography and coda interferometry, *J. Geophys. Res.* **118,** 1067–1078.

Zandomeneghi, D., P. Kyle, P. Miller, I. Passcal, C. Snelson, and R. Aster (2010). Seismic tomography of Erebus volcano, Antarctica, *Eos Trans. AGU* **91,** 53–55.

Zoet, L. K., S. Anandakrishnan, R. B. Alley, A. A. Nyblade, and D. A. Wiens (2012). Motion of an Antarctic glacier by repeated tidally modulated earthquakes, *Nature Geosci.* **5,** 623–626.

Manuscript received 26 January 2021
Published online 12 May 2021